Available online at www.sciencedirect.com
SCIENCE DIRECT
Earth and Planetary Science Letters 248 (2006) 168–185
EPSL
www.elsevier.com/locate/epsl

Temporal variations in slip rate of the White Mountain Fault Zone, Eastern California

Eric Kirby [a,*], Douglas W. Burbank [b], Marith Reheis [c], Fred Phillips [d]

[a] Department of Geosciences, Penn State University, University Park, PA 16802, United States
[b] Department of Earth Sciences and Institute for Crustal Studies, University of California, Santa Barbara, United States
[c] Earth Surface Processes Team, United States Geological Survey, Denver, CO, United States
[d] Department of Earth and Environmental Sciences, New Mexico Tech, United States

Received 14 November 2005; received in revised form 13 May 2006; accepted 20 May 2006
Available online 5 July 2006
Editor: R.D. van der Hilst

Abstract

The evolution of fault slip through time may yield insight into the geodynamics of deforming lithosphere. Precise determination of temporal variations in fault slip is often hindered, however, by a dearth of markers of varying age from which to reconstruct fault slip. Here we determine slip rates across the White Mountain Fault Zone over the past ca. 0.8 Ma from displaced alluvial deposits preserved along the flank of the White Mountains. Displacement histories inferred from deposits containing the ~760 ka Bishop Tuff contrast strongly with those inferred from Late Pleistocene alluvial fans dated by cosmogenic ^{36}Cl, indicating that the fault has experienced significant temporal variations in slip rate. Oblique-slip rates over the past ~760 ky are determined to have been >0.9 m/ky parallel to a net slip vector plunging shallowly (<20°) toward 340°–350°. Displacement of markers in Late Pleistocene alluvial deposits, in contrast, yield slip rates between 0.3 and 0.4 m/ky parallel to a vector plunging somewhat more steeply (20°–40°) toward 320°–340°. These variations in slip rate appear to have operated over timescales >ca. 70 ky, yet occurred on a well-established fault system. Moreover, the timing and magnitude of slip rate variation mimics behavior documented for the northern Fish Lake Valley fault zone. Together, our data provide evidence for coordinated slip rate variations across the Eastern California Shear Zone during the Pleistocene.

Keywords: fault slip rates; Eastern California Shear Zone; active tectonics; cosmogenic radionuclides

1. Introduction

Slip rates on faults, past and present, constitute the observational foundation for understanding the dynamics of lithospheric deformation. Although there has been a historic tendency to interpret fault slip as steady when averaged over multiple seismic cycles, recent studies suggest that interactions among evolving fault networks can significantly modulate the spatial and temporal evolution of fault slip over timescales ranging from 10^5 to 10^6 yr (e.g., [1,2]). Moreover, ascertaining the degree to which fault systems exhibit temporal variations in slip rate is critical for a deeper understanding of geodynamic processes driving crustal deformation. Interpretation of geodetic data in terms of fault slip versus post-seismic transients (e.g., [3]), the degree of crust–mantle coupling, and rheologic

* Corresponding author. Tel.: +1 814 865 0732.
E-mail address: ekirby@geosc.psu.edu (E. Kirby).

0012-821X/$ - see front matter © 2006 Elsevier B.V. All rights reserved.
doi:10.1016/j.epsl.2006.05.026

properties of the lithosphere inferred from fault behavior (e.g., [4]) all depend critically on knowledge of long-term fault slip rates. Determining whether fault displacement rates are time variable remains elusive, however, due in large part to difficulties in developing appropriately precise chronologies of geologic markers that are displaced across a given fault, but have different ages.

In this paper, we utilize well dated stratigraphic and geomorphic markers of varying age to assess temporal variations in slip rate on the White Mountain Fault Zone (WMFZ) over the past 0.8 Ma. The White Mountain fault is one of a series of subjacent faults, including the Owens Valley and Fish Lake Valley fault zones (FLVFZ), that together accommodate right-lateral shear across the Eastern California Shear Zone (ECSZ) [5] between 37° and 38° North latitude. However, the details of how slip is spatially and temporally partitioned among these structures remains uncertain. In particular, the FLVFZ appears to have experienced significant temporal variations in slip rate over the past 1 Ma [6]; we hypothesize that these changes may have been mimicked by variations in slip on the White Mountain–Owens Valley system. Well-preserved deposits of Quaternary alluvium along the western front of the White Mountains allow us to test this hypothesis and yield new insight into the pace and tempo of fault slip in Eastern California.

2. Geologic setting

Active dextral shear between the Basin and Range province and the Sierra Nevada occurs within a 50- to 100-km-wide zone that links deformation in the Walker Lane belt to the north with active faults in the ECSZ to the south. Geodetic studies suggest that shear within this zone accounts for up to 25% of the North America–Pacific relative plate motion (e.g., [7–9]). Between latitudes 37°N and 38°N, most of this shear is accommodated on two main fault systems—the Owens Valley–White Mountain fault system and the Death Valley fault system, of which the FLVFZ is the northernmost portion (Fig. 1). Dextral slip occurred across the FLVFZ at an average rate of ~5 m/ky over the past ~5 Ma [6]. The time of onset of right-lateral shear in the Owens Valley is less certain, but recent thermochronologic studies of the White Mountains suggest significant west-directed extension at ca. 12 Ma, a subsequent period of relative stability, followed by right-lateral, oblique normal slip at ca. 3 Ma [10]. Total displacement since the Pliocene at the northern end of the fault system in Queen Valley appears to be on the order of 1.5–2.5 km [10], yielding average slip rates of approximately 0.5–1 m/ky for the WMFZ.

These average rates, however, belie much of the complexity exhibited by some of these fault systems over shorter timescales. In particular, the FLVFZ appears to

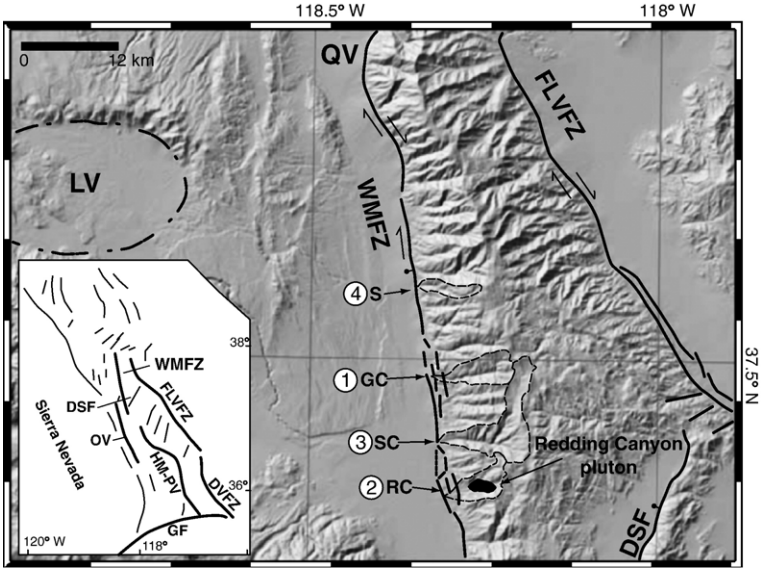

Fig. 1. Tectonic setting of the White Mountain Fault Zone (WMFZ). Abbreviations as follows: DSF—Deep Springs fault, DVFZ—Death Valley fault zone, FLVFZ—Fish Lake Valley fault zone, GF—Garlock fault, HM-PV—Hunter Mountain/Panamint Valley fault zone, LV—Long Valley caldera, OV—Owens Valley fault, QV—Queen Valley. Slip rate sites referred to in text: 1—Gunter Creek, 2—Redding Canyon, 3—Silver Canyon, and 4—Sabies Creek. Watersheds are shown as dashed lines.

have experienced significant temporal variations in slip rate over the past ca. 1 Ma [6]. Disproportionate offset of multiple markers at a single site suggests that right-lateral slip rates may have reached 9–12 m/ky during Middle Pleistocene time (ca. 760 ka) and decreased to 3–5 m/ky during Late Pleistocene time [6,11].

Active faults in the Owens Valley have also been the subject of much interest with regard to the temporal evolution of deformation. On the basis of inversions from fault slip data, Bellier and Zoback [12] suggested a relatively recent (<300 ka) switch from a regional stress regime dominated by E–W extension to one favorable for NW-directed extension. Their argument hinged, to a large degree, on observations of fault striae from the northern Owens Valley fault system [12]. In contrast, Wesnousky and Jones [13] demonstrated that, in fault systems exhibiting slip partitioning between a near-vertical strike-slip fault and a dipping extensional fault, temporal variations in the stress field are not required to explain differences in slip vectors.

The question of what controls the tempo of fault slip has become central to interpretation of recent geodetic data across this region. As has been oft noted, an apparent discrepancy exists across the ECSZ between slip rates inferred from elastic block models of geodetic data [7–9,14] and those determined from geologic data (primarily latest Pleistocene and Holocene deposits). Right-lateral slip rates along the southern Owens Valley fault are well determined (if somewhat debated) to range from ~1 to 3 m/ky on the basis of paleoseismic investigations [15–17]. Farther north along the fault system, right-lateral slip rates for the WMFZ are considerably slower (~0.4 m/ky) [18] and are nearly matched by dip-slip rates (~0.4 m/ky). In contrast, most geodetic models place ~6 mm/yr[1] of right-lateral shear through the valley (e.g., [7]). Although viscoelastic relaxation following the 1872 M 7.5–8 Owens Valley earthquake may help explain this discrepancy [3], the temporal evolution of deformation across the valley remains uncertain.

Whether slip rate variations similar to those observed along the FLVFZ are expressed on faults within the Owens Valley is unknown. As noted above, most studies of faulting in Owens Valley have focused on Late Pleistocene–Holocene deposits and have not sought comparison with longer term measures of fault slip. Such deposits are present along the White Mountain Fault Zone (e.g., [20]), but have not been exploited in detail. Existing estimates of slip rate across the WMFZ rely on an inferred chronology of Holocene deposits with no radiometric control [18]. The first goal of this paper is to provide quantitative estimates of slip rate across the White Mountain Fault Zone over Middle to Late Pleistocene time. Moreover, we seek to understand the causes of temporal variations in slip rate along these fault systems. If changes in slip rate on the FLVFZ are in phase with slip on faults in the Owens Valley, we might seek explanations that invoke changes in external driving forces (e.g., [12]). Alternatively, if slip rate variations are out of phase across the ECSZ, changes in rate may simply reflect local 'switching' of fault systems accommodating more or less constant regional shear strain (e.g., [2]). We test these hypotheses with new estimates of slip rate on the WMFZ over multiple time intervals, ranging from ca. 800 ky to ca. 25 ky.

3. Fault slip data

Preserved along the western flank of the White Mountains (Fig. 1) are a sequence of spectacularly exposed alluvial deposits that range in age from Pliocene to Holocene [18,20,21]. We mapped these deposits for about 40 km along the range front (Fig. 2). We were able to distinguish relative ages of at least five separate alluvial deposits on the basis of preserved surface morphology, the degree of soil and pavement development, and stratigraphic relations. Displacement of stratigraphic and geomorphic markers across the White Mountain Fault Zone provide the basis for estimation of slip rates and associated uncertainties. In this section, we focus on displacement estimates over two time intervals: (1) Middle Pleistocene to present, where age control is provided by airfall deposits of the ca. 760 ka Bishop Tuff [22] and (2) Late Pleistocene to present, where age control is provided by cosmogenic ^{36}Cl dating of alluvial fan surfaces.

3.1. Middle Pleistocene deposits

Mapped geologic relations of alluvial deposits that are interbedded with the Bishop Tuff in two locations along the range front allow us to place bounds on the total displacement across the WMFZ since the Middle Pleistocene. At site 1, near the drainage of Gunter Creek (Fig. 2), up to 10 m of glassy, pumice-rich tephra is interbedded with moderately well indurated alluvial fanglomerates (unit Q_{gc}, Fig. 3). Lueddecke et al. [20] obtained an ^{40}Ar/^{39}Ar age from sanidine from this locality of 0.757±0.004 Ma (Fig. 2), consistent with the

[1] As geodetic and geologic rates measure different aspects of the deformation cycle associated with fault slip [19], we utilize mm/yr to refer to geodetic rates and m/kyr to refer to geologic rates in order to emphasize the timescales over which they are representative.

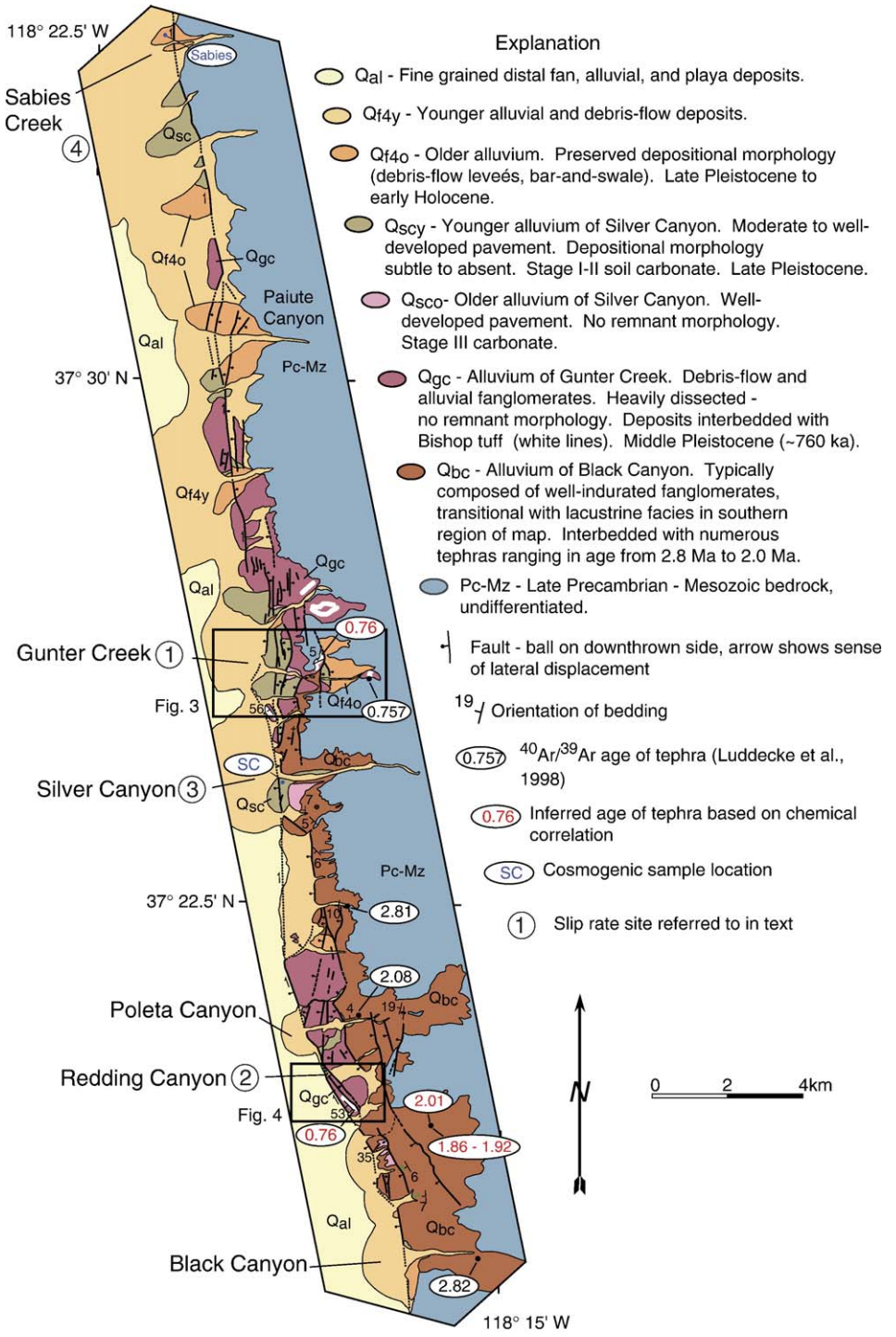

Fig. 2. Geologic map of Pliocene–Quaternary alluvial deposits along the central portion of the White Mountain Fault Zone. White lines represent exposures of the Bishop Tuff.

eruption age of the tuff (~760 ka). We obtained an additional sample from a site ~2 km west for tephrachronology (Fig. 3); geochemical analyses of major elements are a close match for the Bishop Tuff (Table 1), suggesting that the encompassing alluvial fan deposits are approximately ~760 ka. We note that

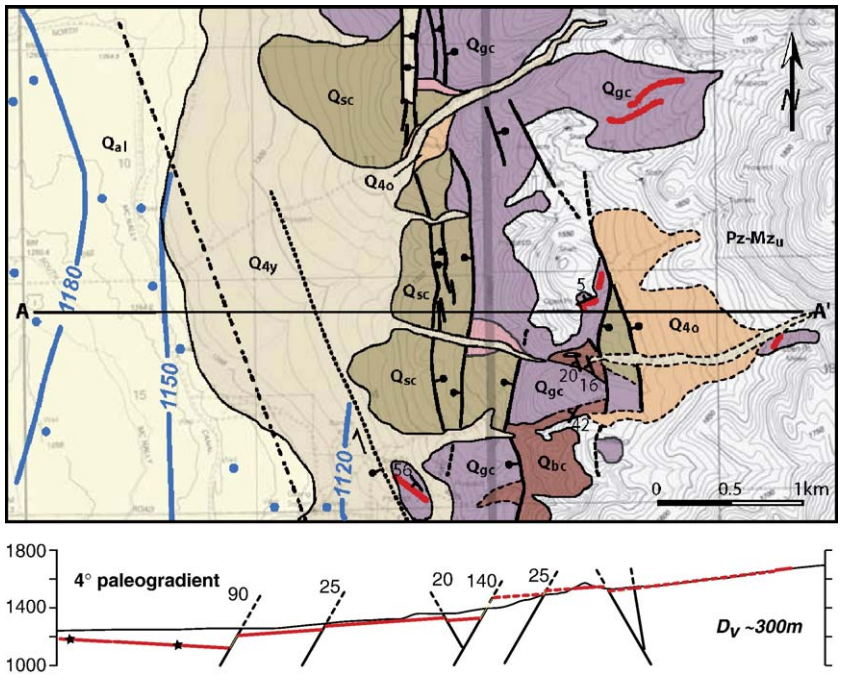

Fig. 3. Geologic map and cross-section of the fault zone at Site 1 near Gunter Creek (see Fig. 2 for location). Unit descriptions are as in Fig. 2. Red lines represent deposits of the Bishop Tuff. Vertical grey line marks a land-use boundary on the USGS topographic base map. Heavy blue lines represent contours of the subsurface elevation (in meters) of the Bishop Tuff (data from Bateman, 1965; blue circles represent the locations of wells that provide local control on the subsurface depth of the Bishop Tuff). Black stars on the cross-section represent the subsurface position of the 1150 m and 1180 m contours on the top of the Bishop Tuff. Vertical separation across the WMFZ is ~400–430 m and places a bound on the normal component of slip along the fault zone since ca. 760 ka. The cross-section represents one permissible reconstruction of normal displacement across the fault zone utilizing a paleo-transport gradient of 4° (see text for details).

locally up to 20 m of alluvium lies stratigraphically above the tuff and likely represents continued accumulation of unit Q_{gc}.

The Bishop Tuff and associated fanglomerates are displaced down-to-the-west along a series of normal and oblique-normal strands of the White Mountain Fault Zone (Fig. 3). The tuff is present in the subsurface beneath the valley, as observed in water wells throughout the northern Owens Valley [21,23]. Correlation of the top of the Bishop Tuff in the subsurface (contours on Fig. 3) with the upper contact of the tuff indicates an apparent vertical separation between deposits in the hanging wall of the WMFZ and deposits stranded in the footwall between 400 and 430 m (Fig. 3).

Reconstruction of fault slip requires some knowledge of the pre-Bishop topographic slope along the range front. The presence of the tuff interbedded with fan deposits indicates that, although deposition of the tuff likely draped a former topographic surface, that surface was actively accumulating sediment. Thus, we can

Table 1
Major-oxide composition and correlation of selected tephra layers from the White Mountain Fault Zone, Owens Valley, CA

Sample	SiO_2	Al_2O_3	FeO	MgO	MnO	CaO	TiO_2	Na_2O	K_2O	Total
Redding Canyon Sample EK-W-02-7 [a]	77.26	12.71	0.76	0.04	0.04	0.46	0.04	3.15	5.55	100.01
Gunter Creek Sample EK-W-02-10 [b]	77.68	12.67	0.74	0.04	0.03	0.45	0.06	3.81	4.52	100.00

Separation, chemical analysis and correlation performed by A. M. Sarna-Wojcicki, U.S. Geological Survey, Menlo Park, CA in 2003.

[a] Pumiceous tephra (>10 m thick) from alluvial deposits comprising shutter ridge along White Mountain Fault Zone near the mouth of Redding Canyon. Deposit has a ~1 m thick, pink middle member. Location: 37°32.727′N, 118°29.600′W. Closest matches are the Bishop Tuff (~0.76 Ma) and the younger suite of the Mono-Glass Mountain ash beds (~0.79–1.2 Ma).

[b] Pumiceous tephra (>5 m thick) interbedded with alluvial deposits near Gunter Creek. Similar deposits ~2 km east were dated by Luddecke et al. (1998) at ca. 0.757 Ma. Location: 37°25.903′N, 118°18.284′W. Closest matches are the Bishop Tuff (~0.76 Ma) and the younger suite of the Mono-Glass Mountain ash beds (~0.79–1.2 Ma).

utilize the top of the Bishop Tuff as a stratigraphic marker of fault displacement, provided we take into account the original transport gradient of the fan. Present-day transport gradients on alluvial fans in the vicinity of Gunter Creek range from 2° to 4° and are consistent with measured bedding attitudes in fanglomerates directly overlying the tuff (~5°, Fig. 3). We estimate paleo-fan gradients of 2–4° that, when combined with uncertainties in depth from the subsurface data [21,23], suggest that vertical displacements of the Bishop Tuff across the fault zone are ~275±25 m. Modeling this net throw across a fault zone with an average dip of 60° (±10°) [10], our reconstruction suggests ~160 m (±40 m) of extension in a direction toward ~270° over the past ca. 760 ky.

Mapped relations and provenance of clasts in alluvial units near Redding Canyon (Site 2, Fig. 1), however, suggest a significant component of lateral displacement during the same time period. Dissected alluvial fans near the mouth of the canyon form a prominent shutter ridge west of the fault zone that has been displaced northward in front of younger fan units (Fig. 4). Locally, fault strands of the WMFZ strike 325°–330° (Figs. 2 and 4). The older alluvium in the shutter ridge is interbedded with well bedded, pumice-rich pyroclastic deposits 3–5 m thick. Geochemical analyses again indicate a close correlation to the Bishop Tuff (Table 1), and thus we consider these alluvial deposits correlative to the remnant fanglomerates at Gunter Creek (Fig. 2).

To estimate displacement of the shutter ridge, we exploited the distinctive provenance of older (Q_{gc}) and younger (Q_{4o}) alluvium sourced from the Redding Canyon watershed (Fig. 4). A small granitic pluton (Redding Canyon pluton [24]) is exposed entirely within the watershed of the canyon and provides essentially a point source of granitic sediment to the alluvial apron along the range (Fig. 1). Although significant portions of the White Mountains expose granitic plutons north of Silver Canyon, the Redding Canyon pluton is the only source of granite in the

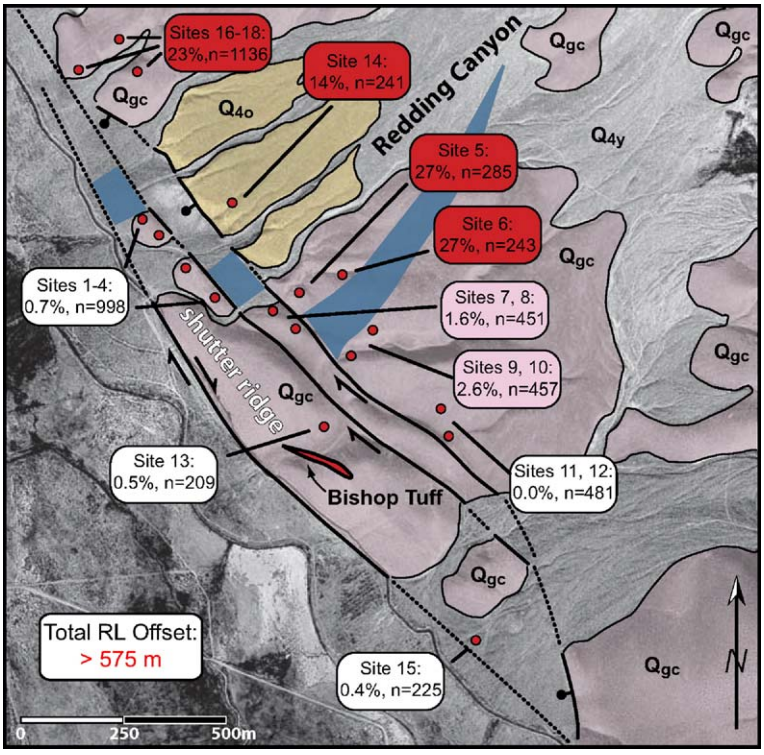

Fig. 4. Geologic map of a shutter ridge of Q_{gc} alluvium along the southern margin of the Redding Canyon alluvial fan (Site 2, see Fig. 2 for location). Red line shows the outcrop trace of interbedded Bishop Tuff. Fan compositions east of the WMFZ display a north–south transition in provenance that reflects granitic material sourced from the mouth of Redding Canyon. Granite-poor composition of the shutter ridge indicates derivation from south of this transition and places a bound on the allowable lateral component of displacement (>575 m in a right-lateral sense). Sample locations for clast composition measurements are shown as red circles (n=number of clasts). The transition from granite-rich alluvium near the axis of Redding Canyon to granite-poor alluvium to the south is shown as a blue wedge and provides a visual representation of the uncertainty on our estimate of lateral displacement.

southern White Mountains [24]. We conducted clast counts from exposures of alluvium in incised drainages in order to avoid bias introduced by preferential weathering of granite on remnant surfaces. Counts were conducted over large regions (>100 m^2) in order to average potential heterogeneity in individual depositional units. Our results reveal a distinct southward decrease in granitic clast percentages (from ~25–30% to ~0–2%) within unit Q_{gc} east of the WMFZ (Fig. 4). The provenance of younger alluvial fans is consistent with a north–south transition from granite-poor to granite-rich material (Fig. 4). West of the fault, however, Q_{gc} gravels within the shutter ridge contain only ~0.5–1% granitic clasts and are juxtaposed against granite-rich gravels to the east. We infer that the shutter ridge must have originated south of the present transition in provenance. The distribution of granitic clasts indicate a minimum of 550±50 m of post-Bishop, right-lateral displacement of Q_{gc} alluvium across the fault (the large uncertainty arises from a lack of exposure between sample sites east of the fault, Fig. 4). We emphasize that this estimate does not account for displacement across the westernmost fault strand and that the northern extent of granite-poor alluvium between fault strands is not exposed. Both factors suggest that the ~550 m of right-lateral offset represents a conservative estimate of the minimum amount of right-lateral slip since the mid-Pleistocene.

3.2. Late Pleistocene deposits

Displacement across the WMFZ since Late Pleistocene time was determined using vertically-displaced alluvial fan surfaces and laterally-offset debris-flow levees at two sites along the fault zone (Fig. 2). At Silver Canyon (Site 3, Fig. 1), an abandoned fan surface is displaced down to the west along a single strand of the WMFZ. Additional mapped faults within the range [10] do not displace correlative terrace deposits along the northern wall of Silver Canyon (Fig. 2), and we are confident that this site provides a reasonable estimate of net vertical displacement across the WMFZ.

We surveyed topographic profiles across the fault scarp using a high-precision differential GPS, summed the observed vertical displacements, and estimated net horizontal extension by modeling a range of possible fault dips. Total uncertainties were estimated using a Monte Carlo routine incorporating uncertainties in fan surface slope, projection errors, and dip of the fault (here assumed to be 60°±12° at 2σ) [25]. Of these, uncertainty in fault dip dominates the total. We sum extension across the fault, rather than the total vertical separation, because the presence of a subsidiary antithetic scarp (Fig. 5) leads to a reduction in the net vertical separation across the fault zone. Simple kinematic rules (conservation of cross-sectional area), however, demand that this slip be accommodated at depth, however, and thus the total extension is a robust measure of net fault slip. Survey results indicate ~8.2±2.1 m of extension across the primary fault scarp; subsidiary faults contribute another ~2 m leading to a net extension of 10.2±2.1 m across the fault zone (Fig. 5A).

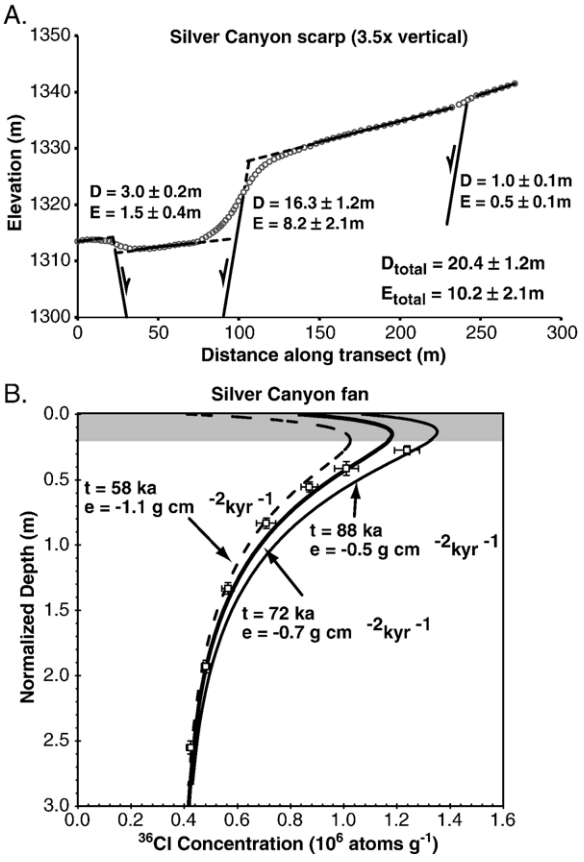

Fig. 5. Displacement across the White Mountain Fault Zone during Late Pleistocene time at Silver Canyon (Site 3, Fig. 2). (A) Topographic profile and reconstructed fault displacement based on projection of preserved fan surface and assumed fault dip. Uncertainties reflect a Monte Carlo propagation of uncertainty in fan slope, fault dip, and projection. We use estimates of net horizontal extension (E), with their associated uncertainties, to model the total fault slip on a single plane at depth (see text for details). (B) Fit of calculated ^{36}Cl concentration with depth to Silver Canyon (WAC01-01) normalized depth profile ^{36}Cl data. "t" is the exposure time, "e" is the surface erosion rate (negative values indicate profile aggradation). The "t=72 ka" curve is the best-fit profile and the "t=88 ka" and "t=58 ka" curves are the fits at the one-standard-deviation limits of the $\Delta\chi^2$ criterion (see appendix for details). Results suggest a depositional age of the fan surface of 72±15 ka.

Table 2
Chemistry, particle size (USDA units), and field notes for soil pit at Silver Canyon

Horizon or unit	Depth (cm)	Field gravel (%)	Lab gravel (%)	$CaCO_3$ (%)	Soluble salts (%)	Bulk density, total (g/cm^3)	Bulk density, <2 mm (g/cm^3)	Sand 2000–50 μm	Silt 50–2 μm	Clay <2 μm
Av	0–6	15	28	3.23	0.03	1.31	1.26	95.81	3.26	0.94
Bwk/Av	6–15	15	17	4.27	0.03	1.64	1.32	85.25	11.83	2.92
Bwk2	15–36	20	61	2.15	0.05	1.50	1.32	88.95	8.37	2.67
Bwk3	36–77	60	65	15.63	0.04	1.81	1.57	92.47	6.88	0.65
2Bk1	77–120	80	78	10.37	0.04	2.13	1.51	95.74	3.84	0.41
2Bk2	120–182	85	72	12.35	0.06	1.80	1.60	95.85	3.77	0.38
3Bk3	182–265	85	71	11.55	0.04	2.10	1.50	91.62	7.72	0.66

Horizon [a]	Depth (cm)	Dry color	Moist color	Structure [b]	Dry consistence [c]	Wet consistence [d]	Clay films	Stage $CaCO_3$ [e], other
Av	0–6	10YR7/3	10YR5/4	2f–m sbk	so	so, po	0	0, ev
Bwk/Av	6–15	10YR7/2	10YR5/4	2f–m sbk	so	ss, vps	0	I, es
Bwk2	15–36	10YR7/3	10YR6/4	3f–c sbk	sh	ss, vps	0	II, es–ev
Bwk3	36–77	2.5Y8/3	2.5Y6/3	2f–m abk, 1m–c pl	h	ss, vps	0	II+, ev; small
2Bk1	77–120	2.5Y7/3	2.5Y5/3	sg–m	lo–h	so, po	0	I+, e–es
2Bk2	120–182	2.5Y7/2	2/5Y5/3	sg	lo	so, po	0	I, e; small spots SiO_2
3Bk3	182–265	2.5Y7/3	2/5Y5/3	sg	lo	so, po	0	I−, e; small spots SiO_2

[a] Horizon nomenclature and carbonate stage follow Birkeland [50] and references therein.
[b] Structure codes: strength/abundance: 1–3. Size: f, fine; m, medium; c, coarse. Shape: sbk, subangular blocky; abk, angular blocky; pl, platy; s.g., single grain; m, massive.
[c] Dry consistence codes: lo, loose; so, soft; sh, slightly hard; h, hard.
[d] Wet consistence codes: so, non-sticky; ss, slightly sticky; po, non-plastic; vps, very slightly plastic.
[e] Carbonate codes: e, effervesces weakly; es, effervesces strongly; ev, effervesces violently.

Table 3
Cosmogenic ^{36}Cl data for Silver Canyon depth profile and Sabies Canyon boulder samples

Sabies Canyon Boulders: (37.57897°N, 118.3506°W; 1560 m)	S_T (unitless)	q_v (unitless)	Depth (g/cm^2)	$^{36}Cl/Cl$ ($\times 10^{15}$)	Model age [a] (ka)	Model age [b] (ka)	Model age [c] (ka)
Sabies A	0.9974	0.005	0	261±11	27.8±1.3	25.8±1.1	23.6±1.0
Sabies C	0.9974	0.005	0	558±26	44.5±2.3	40.7±2.0	37.5±1.8
Sabies E	0.9974	0.005	0	3120±190	30.0±1.9	30.3±1.9	31.2±2.1
Sabies F	0.9974	0.005	0	1570±77	32.3±1.7	32.1±1.6	32.1±1.7
Sabies G	0.9974	0.005	0	195±9	23.8±1.3	22.3±1.1	20.6±1.0
Sabies J	0.9974	0.005	0	585±26	99.4±5.1	86.8±4.1	84.9±4.6

Silver Canyon Soil Profile: (37.40386°N, 118.3145°W; 1352 m)	S_T (unitless)	q_v (unitless)	Depth (g/cm^2)	Meas. ^{36}Cl conc. (10^5 atoms/g)	Norm. ^{36}Cl conc. (10^5 atoms/g)
Wac-01-1 35–40	0.998	0.08	61.5	13.1±0.49	12.4±0.46
Wac-01-1 50–65	0.998	0.08	91.0	10.1±0.44	10.1±0.44
Wac-01-1 70–80	0.998	0.08	125	8.36±0.29	8.71±0.31
Wac-01-1 100–109	0.998	0.08	188	6.80±0.36	7.08±0.37
Wac-01-1 145–155	0.998	0.08	301	5.64±0.23	5.64±0.23
Wac-01-1 195–205	0.998	0.08	436	4.69±0.16	4.81±0.17
Wac-01-1 250–260	0.998	0.08	576	4.15±0.15	4.24±0.16

S_T is the topographic shielding factor and q_v is the volumetric water content.
[a] No erosion of boulder surface.
[b] 1.1 mm/ky erosion rate.
[c] 3.3 mm/ky erosion rate.

Table 4
Chemical data for Silver Canyon depth profile and Sabies Canyon boulder samples

	SiO_2 (wt. %)	TiO_2 (wt. %)	Al_2O_3 (wt. %)	Fe_2O_3-T (wt. %)	MnO (wt. %)	CaO (wt. %)	MgO (wt. %)	Na_2O (wt. %)	K_2O (wt. %)	P_2O_5 (wt. %)	LOI (wt. %)	Cl (ppm)	B (ppm)	Gd (ppm)	U (ppm)	Th (ppm)
Sabies Canyon Boulders																
Sabies A	61.13	0.65	16.79	6.23	0.07	3.06	2.83	4.18	3.15	0.06	1.70	257	13	4	2	9
Sabies C	75.06	0.29	13.31	1.60	0.01	0.29	0.30	3.60	5.15	0.02	0.73	176	7	4	2	18
Sabies E	91.11	0.24	3.70	2.75	ND	0.01	0.46	0.25	0.75	0.02	0.61	1.66	20	2	1	1
Sabies E (dup)	90.68	0.24	3.69	2.73	ND	0.01	0.47	0.25	0.75	0.01	0.61	ND	ND	ND	ND	ND
Sabies F	91.95	0.20	3.74	1.62	ND	0.01	0.45	0.34	0.68	0.07	0.69	3.52	23	2	1	1
Sabies G	62.39	0.78	17.34	5.17	0.06	2.52	2.41	4.78	3.03	0.08	1.67	331	38	3	3	11
Sabies J	60.64	0.60	16.05	6.37	0.10	5.83	2.79	3.48	2.23	0.05	1.47	400	68	4	2	12
Silver Canyon Soil Profile																
Wac-01-1 35–40	67.39	0.87	15.34	5.85	0.04	1.85	0.35	3.39	1.84	0.03	2.74	24.3	43	6	4	14
Wac-01-1 50–65	65.95	0.94	16.01	6.57	0.04	1.96	0.13	3.51	1.66	0.03	2.81	17.2	45	5	3	14
Wac-01-1 70–80	66.99	1.00	15.61	6.36	0.04	1.81	0.15	3.41	1.83	0.03	2.75	16.7	43	6	3	15
Wac-01-1 70–80 (dup 1)	66.98	1.00	15.61	6.37	0.04	1.82	0.15	3.39	1.82	0.03	2.75	ND	ND	ND	ND	ND
Wac-01-1 70–80 (dup 2)	67.24	1.00	15.62	6.40	0.04	1.82	0.15	3.41	1.83	0.03	2.75	ND	ND	ND	ND	ND
Wac-01-1 100–110	66.62	1.00	15.72	6.47	0.04	1.93	0.11	3.47	1.84	0.03	2.77	28.0	46	7	3	15
Wac-01-1 145–155	66.13	1.03	15.84	6.74	0.04	2.00	0.15	3.41	1.85	0.03	2.85	19.2	41	5	3	11
Wac-01-1 145–155 (dup)	65.97	1.04	15.82	6.75	0.04	2.00	0.16	3.41	1.84	0.03	2.85	ND	ND	ND	ND	ND
Wac-01-1 195–205	65.56	1.07	16.07	6.78	0.04	1.89	0.13	3.41	1.83	0.03	2.84	38.4	46	6	4	11
Wac-01-1 250–260	65.11	1.05	16.18	6.95	0.04	1.97	0.12	3.46	1.77	0.03	2.89	32.9	48	6	3	10

LOI is loss on ignition, “dup” indicates duplicate sample, and ND indicates “not determined”.

We estimate the ages of the displaced fan surface from both soil development and cosmogenic ^{36}Cl concentrations in a depth profile. The fan surface exhibits a moderately well developed desert pavement, with abundant varnished clasts preserving only subtle remnant depositional forms (unit Qsc, Fig. 2). We excavated a 3 m deep soil pit in this surface and characterized the degree of soil development (Table 2). The fan surface exhibits a moderately well-developed soil with stage II+ pedogenic carbonate developed in the Bk horizon and a profile development index [26] value of ~26, similar to those of soils on surfaces dated between 30 and 60 ka in the western U.S. (e.g., [27,28]).

In order to refine this estimate, we collected a depth profile of 7 samples for ^{36}Cl dating [29]. Analytical protocols are available in Appendix A and corresponding data can be found in Tables 3 and 4. Cosmogenic ^{36}Cl samples exhibit an exponential decrease in concentration with depth (Fig. 5B) that allows relatively unambiguous interpretation of the inherited component of the present-day inventory (see appendix for details). Concentrations at depths of 2.5–3 m indicate a mean inheritance equivalent to ~29 ky of exposure (Fig. 5B). Our interpretation of the age of the surface depends on the rate of accumulation of ~25 cm of eolian sediment in near-surface horizons. The profile age and age uncertainty were calculated by means of χ^2 fitting [30] to modeled ^{36}Cl distribution with depth. We allowed both the surface age and net aggradation rate to vary as free parameters (see appendix for details) and modeled a range of geologically-reasonable dust accumulation rates. Based on the goodness of fit of modeled ^{36}Cl concentration to the observed data (Fig. 5B), we obtained an age of 72±15 ka for the deposition of the surface, with a preferred aggradation rate of 0.7 g/cm^2 ky.

Evidence for significant lateral slip across the WMFZ is indicated by the presence of shutter ridges and displaced drainages along the length of the fault zone (Fig. 2). However, we were only able to quantitatively estimate displacement rates at a site near Sabies Canyon (Site 4, Fig. 1), near the northern end of our study area. This fan preserves significant depositional morphology in the form of prominent bar-and-swale and debris-flow levees. Soil development is relatively immature (azonal), although pavement is moderately well-developed on top of a 3- to 5-cm-thick Av horizon (unit Qf4o, Fig. 2). Active slip on the WMFZ in this segment is confined to a single strand (Fig. 2) that displaces debris-flow levees and channels in a right-lateral sense (Fig. 6A). Based on differential GPS surveys (Fig. 6A, inset), the levees appear to be displaced 8±1 m.

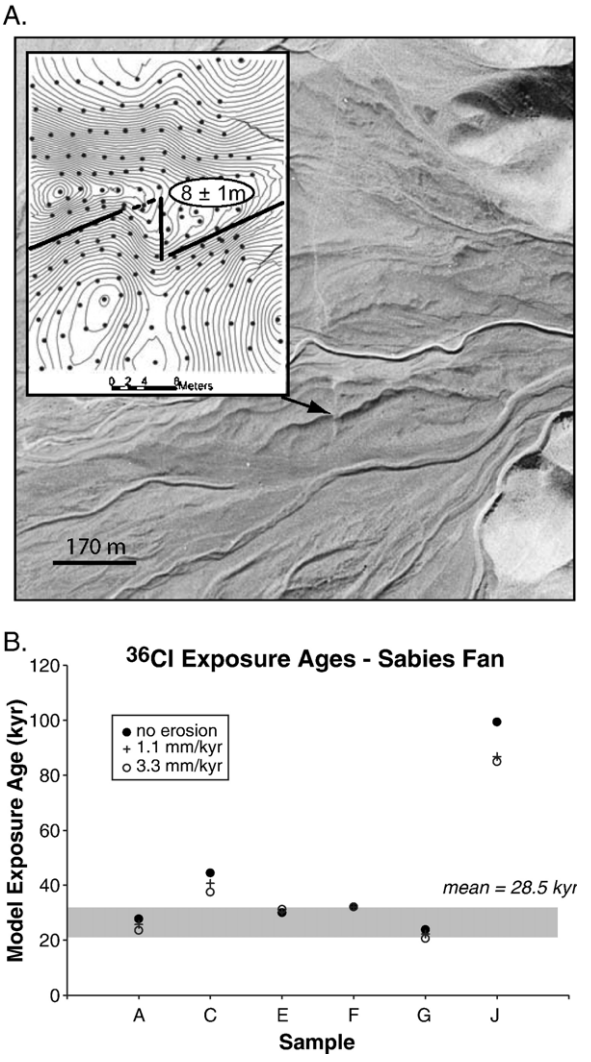

Fig. 6. Lateral displacement of boulder levee at Sabies Canyon (Site 4, Fig. 2). (A) Air photo of right-laterally displaced debris-flow levee on the Sabies Creek fan. Inset shows topographic map developed from differential GPS surveys (0.1 m contour interval, arbitrary datum). The levees are displaced by 8±1 m. (B) ^{36}Cl exposure ages for boulders at the Sabies Creek site. Ages are modeled for a range of weathering rates and mass loss from the boulder surface (0, 1.1, and 3.3 mm/ky). Two samples yielded anomalously old ages that are attributed to inheritance at the time of deposition. The range of ages for the remaining 4 samples suggest that the boulder levee was likely deposited between 22 and 32 ka. The absence of evidence for post-depositional erosion of the debris-flow surface suggests that the younger end of this range should most closely represent the age of the surface (see text for details).

In a previous study, DePolo [18] inferred from surface and soil development that the fan was of Holocene age. To test this interpretation, we collected 6 samples from large (>1 m diameter) boulders present atop a large channel levee and dated each independently

using ^{36}Cl. Analytical data are given in Tables 3 and 4. The interpretation of exposure ages of boulders may be complicated by several factors, including (1) exhumation of previously buried boulders, (2) weathering and loss of material from the boulder surface, and (3) inheritance in the boulders themselves. The relative preservation of the immature soil atop the fan surface coupled with the size of the boulders suggest that (1) is not an important factor at this site. In order to account for weathering of the boulder surface, we modeled exposure ages as a function of weathering rates between 0 and 3.3 mm/ky (Table 3), consistent with previous work on Sierran alluvial fans [28].

The results of ^{36}Cl exposure ages on large boulders at the site yield a range of ages from ~20 ky to ~65 ky (Table 3). Two of these samples are distinct outliers (Fig. 6B); we attribute these to inheritance and exclude them from the following discussion. The remaining 4 samples all yield exposure ages between 22 and 32 ky. As argued above, burial and subsequent stripping of the surface does not appear likely at this site. The youngest sample, therefore, should most closely reflect the time of deposition of the levee (i.e. have the least inheritance). Exposure ages modeled as a function of weathering of the boulder surface for this sample yield exposure ages between 21 ka and 24 ka (Table 3); we take these as the best estimate of the age of the levee.

4. Slip rate variation through time

Measurements of extension at the Gunter Creek site and lateral slip at Redding Canyon allow us to place bounds on the slip vector across the fault zone. Although we acknowledge the possibility of displacement gradients along strike (e.g., [31]), the sites are only separated by ~10 km (Fig. 2), and are located near the center of the fault where displacement gradients are expected to be minimal. Thus, we presume that along-strike variations between the sites are small relative to the ~100-km strike length of the fault system. In order to determine a net slip vector that is consistent with our estimates of lateral and vertical displacement, we resolve both onto a single plane parallel to the overall strike of the fault zone (~350°). We incorporate uncertainties arising from displacement estimates and from analytical uncertainties on surface ages. For simplicity we first consider the projection of displacement in the horizontal plane (Fig. 7).

Geologic relationships at the Redding Canyon shutter ridge (Site 2) indicate a minimum of 550± 50 m of right-lateral displacement across a fault striking ~330°. Combined with the age of the Bishop Tuff

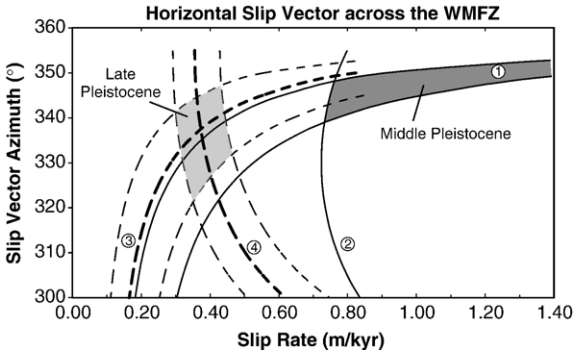

Fig. 7. Comparison of horizontal displacement rates determined across the White Mountain Fault Zone from Middle Pleistocene (solid lines) to Late Pleistocene time (dashed lines). The ordinate represents the map projection azimuth (360°=north) of the net displacement vector across the fault zone, while the abscissa represents displacement rate (in m/ky). Constraints from slip rate sites are referenced as in text (Site 1—Gunter Creek, Site 2—Redding Canyon, Site 3—Silver Canyon, Site 4—Sabies Canyon). Heavy dashed lines represent mean values for Late Pleistocene markers and light dashed lines represent the range of allowable values. Solid lines represent allowable values for Middle Pleistocene markers (note that the mean is excluded for clarity). Because the lateral slip at Redding Canyon (Site 2) is a minimum bound, only one curve is shown. The intersection of the curves defines fields in which the allowable slip vectors may lie. Note that average displacement rates since the Middle Pleistocene appear to have been 2–3 times greater than during the Late Pleistocene.

(~760 ka), these relationships suggest a local right-lateral slip rate in excess of 0.7–0.8 m/ky. Net extension across the fault zone at Gunter Creek is estimated at 160±40 m (normal to faults striking ~360°), yielding extension rates between 0.15 and 0.25 m/ky. A graphical estimate to the best fit slip direction that satisfies both of these constraints is shown in Fig. 7. We estimate that the average horizontal displacement rate over the past ~760 ky has been >0.75 mm/yr in a direction toward 340°–350°.

A similar analysis for displacement rates over Late Pleistocene time, in contrast, yields significantly different results. Using the age of the fan surface at Silver Canyon (72±15 ka) and the range of allowable extension (10.3±2.1 m) yields horizontal extension rates (toward 270°) between 0.1 and 0.2 m/ky. Lateral offset of the debris-flow levees at Sabies Canyon (8± 1 m), combined with our estimate of the age of the deposit (22.5±1.5 ka) yields right-lateral slip rates of 0.3–0.4 m/ky (parallel to local fault strike—355°). Allowable slip rates that satisfy both these criteria range from 0.3 to 0.45 m/ky and from 320° to 345° in azimuth (Fig. 7). These rates are consistent with slip rates previously inferred by DePolo [18].

To this point, we have limited our discussion to the horizontal projection of the displacement vector across

the WMFZ. Resolution of the lateral and fault-normal components of slip considered above parallel to the net slip vector across the fault zone (striking 350° and dipping 60°±10°) yields an average oblique-slip rate >0.9-1.2 m/ky since the Middle Pleistocene. Average oblique-slip rates over Late Pleistocene time are significantly lower, and range from 0.37 to 0.57 m/ky (minimum and maximum allowable rates). We note that, although uncertainties on the trend of the slip vector do not permit confident resolution of a difference in displacement direction (Fig. 7), slip rates appear to be significantly different between Middle and Late Pleistocene times. We have been conservative in the propagation of uncertainties, and even the maximum allowable slip rate for the Late Pleistocene lies outside the minimum rate since Middle Pleistocene time. Thus, we conclude that the White Mountain Fault Zone has experienced temporal variations in slip rate through time.

5. Tectonic implications

Our results indicate that slip rates on the White Mountain Fault Zone have varied by a factor of 2–3 over the past 800 ky. Although we have combined separate estimates of lateral and horizontal displacement rates, the similarity between resolved slip vectors averaged over the past 60–90 ky (320°–340°) and vectors inferred from geodetic measurements for present day displacement across the ECSZ (323°±5°) [7] give us a measure of confidence that our estimates capture the displacement rate (0.3–0.45 m/ky) across the fault zone during the Late Pleistocene. In contrast, both the displacement vector and rate appear to have been different when measured over the past ~760 ky. Slip rates are estimated to have exceeded 0.9 m/ky and the displacement vector appears to have been somewhat shallower (trending 340°–350°). Thus, our data imply that slip rates must have decreased at some point prior to or during the Late Pleistocene (ca. 70 ka). Although we are unable to precisely resolve when this decrease in rate occurred, the fact that younger deposits yield slower rates indicates that this result is not an artifact of sampling interval (e.g., [32]).

Available paleoseismic data from the White Mountain Fault Zone are sparse, but existing estimates of the timing and extent of recent surface ruptures lend some insight into the possibility of clustered seismicity associated with slip rate variations (e.g., [19]). DePolo [18] recognized that the most recent large surface rupture along the WMFZ was associated with fresh, single-event scarps preserved over ~16 km of the central and southern portion of the fault zone. The maximum observed displacement is ~3.5 m of primarily normal-sense slip, and modeling of scarp degradation suggests the event occurred approximately 1–3 ka [18]. If such events are characteristic of ruptures along the WMFZ, the observed normal component of displacement at Silver Canyon (~20 m, see Fig. 5) would require 4–5 events. Although this inference is tentative, an even greater frequency of rupture prior to ~70 ka would be required to explain increased slip rates during this interval. Alternatively, the rupture identified by DePolo [18] may underestimate the extent of Late Pleistocene ruptures. We consider the inference of variations in slip rate to thus provide strong motivation for future investigations into the paleoseismicity of the White Mountain Fault Zone.

Temporal variations in slip rate on the WMFZ mimic those observed on the subparallel FLVFZ (Fig. 1); displacement of deposits containing the Bishop Tuff suggest right-lateral slip rates as high as 10–12 m/ky during the Middle Pleistocene, whereas displaced latest Pleistocene units indicate rates between 2 and 4 m/ky [6]. Although the FLVFZ exhibits systematically higher displacement rates during both time intervals, the magnitude of rate variation (3- to 5-fold) is similar between both fault systems. Additionally, circumstantial evidence suggests that other fault systems in the region also experienced rapid displacement following the eruption of the Bishop Tuff (e.g., Deep Springs fault [11], e.g., Deep Springs fault [33]). Thus, throughout this portion of the ECSZ, slip rates on multiple individual faults appear to have varied in concert, strongly suggesting that the entire system was modulated by an external forcing.

The nature of that forcing remains uncertain. The timescale of transient deformation appears too short to reflect variations in plate boundary forces. Although our data are consistent with the hypothesis of Bellier and Zoback that regional variations in the stress field occurred during the Pleistocene [12], our resolved slip vectors imply greater rates of lateral displacement during the Middle Pleistocene. This result is counter to their inferred stress change that would predict greater lateral slip post ca. 300 ky [12]. Perhaps such changes are cyclic, but our data are not sufficiently distributed through time to test this hypothesis.

Conversely, the tempo of variation in fault slip appears somewhat long relative to recognized examples of clustered seismicity. Clustered strain release has been

inferred from paleoseismic records throughout the Mojave segment of the ECSZ [34] and in the Basin and Range [19], and may result from fault array interaction over timescales of $\sim 10^4$ yr. As noted above, if seismic events are clustered in time, they would have been associated with intervals of time $> \sim 70$ ky in order to explain observed slip rate variations.

We speculate that the origin of coordinated variations in slip rate across this portion of the Eastern California Shear Zone may reflect the local influence of the Long Valley caldera system. We follow Gillespie [35] in suggesting that stress changes associated with eruption of the Bishop Tuff and subsequent collapse of the caldera may have facilitated rapid fault slip. Surface loads are known to significantly influence fault displacement (e.g., [19,36]), and we hypothesize that magma chamber evacuation may have reduced normal stresses across faults in this portion of the ECSZ, modulating fault slip throughout the region. Such a mechanism has been proposed for a correlation between earthquakes in the Apennines and eruptions of Vesuvius [37]. We note that, in this study, evacuation of a 0.1 km^3 magma chamber was sufficient to impact Coulomb stresses on fault systems up to 50 km distance. Eruption of the Bishop Tuff is estimated to have evacuated a volume of magma in excess of ~ 600 km^3 [38], and it seems only plausible to suggest that this event significantly influenced regional stress fields.

Finally, although this mechanism may provide a potential explanation for high slip rates inferred from deposits of Bishop age, it does not adequately explain the low slip rates across the ECSZ during Late Pleistocene time. Our observations are consistent with the lower range of slip rates determined for the Owens Valley fault (~ 1 m/ky [15,17]) and confirm previous suggestions that much of the lateral slip on the Owens Valley fault is transferred northward onto the White Mountain fault system (e.g., [11]). These results also strengthen the argument for a significant discrepancy between geologic slip rates and geodetic velocities. Together, Late Pleistocene lateral slip rates across the Owens Valley–White Mountain fault system (0.5–1 m/ky) and the Fish Lake Valley fault zone (2–3 m/ky, [6]) account for $<50\%$ of the geodetically-measured velocities across the ECSZ [7]. The mismatch does not appear to result from inadequate chronology or imprecise geologic data on the large fault zones, but rather must reflect some combination of post-seismic transient deformation [3] and/or distributed strain across the Owens Valley.

6. Conclusions

New mapping and chronologic studies of late Quaternary deposits along the White Mountain Fault Zone form the basis for a refined estimate of slip rates through time. Resolution of displacement vectors from displaced Middle Pleistocene and Late Pleistocene alluvial deposits indicate that oblique-normal slip rates across the fault zone were highest (>0.9 m/ky) during the Middle Pleistocene, following eruption of the Long Valley caldera. Rates decreased at some point before or during the Late Pleistocene by a factor of 2–4. Rate variations mimic those previously inferred for the Fish Lake Valley fault zone, and together our data suggest that both major fault systems in this portion of the Eastern California Shear Zone experienced in-phase variations in slip rate. Thus, it appears that external forcing may significantly modulate regional strain fields at timescales longer than earthquake cycles, yet shorter than the life span of individual fault systems.

Acknowledgments

This research was supported by NSF grants EAR-0196321 and EAR-0409169. We thank Nancye Dawers, Kevin Furlong, Mike Oskin, and Doug Walker for productive discussions on this and other aspects of Eastern California. A thoughtful review by Anke Fredrich significantly improved aspects of the discussion. Margaret Berry, John Caskey, Craig Jones, Mike Machette, and Paul Zehfuss all provided comments on a previous version of this manuscript.

Appendix A. Cosmogenic ^{36}Cl analytical protocols and age interpretation

A.1. Depth-profile sampling and analysis

Gravel samples for ^{36}Cl analysis were collected from the walls of soil pits. The target depth for the pits was ~ 3 m in order to provide a complete profile from which the amount of inheritance could be accurately measured. Depth was measured using a steel tape and samples of gravel were scraped from the wall of the pit in horizontal bands that ranged from 5 to 10 cm in the vertical dimension, depending on the availability of suitable-sized clasts. In the field, the material excavated was put through nested sieves having meshes of 12.7 and 6.35 mm, with the trapped clasts being retained for analysis. Sufficient material was excavated to provide ~ 500 g of sieved gravel, yielding ~ 250 individual

clasts. These clasts were pulverized to provide a representative average ^{36}Cl concentration for each depth interval, inasmuch as individual clasts may have experienced widely varying exposure histories prior to being buried in the deposit. In the field, the horizon shielding was measured using a compass and hand level and the surface slope and aspect were recorded. Soil bulk densities were measured for each logged soil horizon using either the clod method for cohesive, fine-grained horizons or the excavation method for loose and/or coarse horizons [39].

The pulverized 500-g samples were ground and sieved to retain the fraction between 0.15 and 1 mm. The retained fraction was thoroughly mixed to ensure homogeneity. The ground rock was leached in 3% nitric acid to remove any pedogenic carbonate. Aliquots were then removed for analysis of major elements, U, and Th by X-ray fluorescence and for analysis of B and Gd by gamma emission spectrometry. The remaining rock was dissolved in a mixture of HF and HNO_3 in Teflon bottles. After dissolution was complete, the fluorosilicate solids that precipitated during the dissolution were removed by centrifugation and a ^{35}Cl spike was added, followed by $AgNO_3$ in order to precipitate AgCl. The AgCl was purified of S and submitted to the Purdue Rare Isotope Measurement Laboratory (PRIME Lab) where the $^{36}Cl/^{35}Cl$ and $^{35}Cl/^{37}Cl$ ratios were measured by accelerator mass spectrometry (AMS) [40,41]. The Cl concentration of the sample was calculated from these data using the principles of isotope-dilution mass spectrometry. Detailed information on sample preparation can be found in [42].

Analytical results are given in Table 3. Radiogenic ^{36}Cl concentration (that was produced by absorption of fissionogenic neutrons and (α,n) reaction neutrons by ^{35}Cl) was calculated according to [43] and subtracted from the measured ^{36}Cl concentrations to calculate the cosmogenic ^{36}Cl. Results of the chemical analyses are presented in Table 4. Average compositions of each profile were used in the dating calculations described below. The ^{36}Cl concentrations of the individual samples were normalized to the profile average for purposes of comparison.

A.2. Profile age computation

The samples from each depth horizon do not necessarily have the same lithology, and hence the chemical composition and the ^{36}Cl production rate may vary from sample to sample. In order to compare the results from the different depths, it is necessary to normalize the sample compositions. This was accomplished as described below.

(1) The bulk densities are multiplied by the depths to produce a table of cumulative mass per unit area as a function of depth. Using this table, each sample is assigned a mass depth (i.e., depth in g/cm^2) representative of the layer sampled.
(2) Using the measured chemical compositions, the ^{36}Cl production rate (at the land surface) is calculated for each sample. These production rates are averaged and the sample closest to the mean is used as the basis for normalization, so long as it is not an outlier in terms of its ^{36}Cl concentration.
(3) The production rate of each sample is computed at its actual sample depth, then the production rate for the normalization sample is also computed at the same depths. The production rate for each sample is divided by the production rate for the normalization sample to obtain the normalization factor.
(4) The measured ^{36}Cl concentration at each depth is multiplied by the normalization factor for that depth to obtain the normalized concentration.

The soil age was determined by fitting a calculated ^{36}Cl inventory versus depth to the measured, normalized, profile. The best-fit match was estimated by minimization of the reduced χ^2 computed from the differences of the calculated and measured values. Uncertainties in the ages were also calculated from the χ^2 variation, described in more detail below. The theoretical ^{36}Cl inventories with depth were calculated using the spreadsheet model CHLOE [44]. CHLOE is based on the cosmogenic nuclide production equations given by [45]. The high-energy cosmic-ray flux is calculated on the basis of standard exponential attenuation with mass depth and a spallation production rate proportional to that flux. The model then uses this flux distribution as the source term for the calculation of the epithermal and thermal neutron fluxes by means of the diffusion equations given in [46]. The spatial distributions of low-energy neutron fluxes are then used to calculate the ^{36}Cl production by epithermal and thermal neutron absorption. Nuclide production parameters from [46] were employed, whereas use of alternative production parameters by [47,48] would give ages that are younger by approximately 15%.

In general, soils developing on non-eroding surfaces can be considered stable over geologic time. In

the geomorphic environment of the Silver Canyon sample site (an alluvial fan), parent material is typically deposited by debris flows and fluvial action at a fairly rapid rate so long as the site remains in the depositionally active area of the alluvial fan [49]. When alluvial deposition ceases, the surface stabilizes and pedogenic processes begin to operate. In arid regions, the early stages typically are dominated by atmospheric deposition, with the result being accumulation of eolian dust, including silt, clay, calcium carbonate, and locally salts, in the soil profile [50]. Even in relatively humid climates, soils often show considerable net accumulation [51]. A significant proportion of the dust is accumulated as a distinct layer on the surface of the parent material (Av horizon), protected by a stone (desert) pavement [52], but most of the calcium carbonate and some of the silt and clay infiltrates into the profile and accumulates in the top 50–100 cm [50]. Eventually, accumulation of these materials plugs the pore space and runoff begins to increase, leading to enhanced erosion and stripping of the soil fines [53]. This stripping is confined to the surface of the soil.

CHLOE simulates erosion using classical cosmogenic nuclide formulations (e.g., [45]), which assume that erosion is from the surface. Analogous equations are not commonly used for the case of aggradation because there is no fixed relation between the cosmogenic nuclide concentration of sediment deposited on top of a geological unit and that of the material in the unit. However, for the material we are analyzing this is not an issue because aggradation results from atmospheric deposition and the products of the deposition (mainly silt and calcium carbonate) are separated from the parent material being analyzed by sieving and acid leaching. We therefore analyze none of the accumulation resulting from atmospheric deposition. However, the classical equations, when used for aggradation, treat the process entirely as deposition on the surface. This is true for part of the actual atmospheric deposition (the silt cap), but not for the pedogenic calcite and silt that infiltrates the profile. This may to some extent affect the outcome of the fitting process, but probably not to an extent that is large compared to the other uncertainties.

Given that the alluvial fan surface at Silver Canyon (Site 3) exhibits high concentrations of silt in the upper 15–25 cm of the profile (Table 2), it is clear that, as expected, the profile has undergone net aggradation. With a measured bulk density of 1.31 g/cm^3, this amounts to 46 g/cm^2 over ~70 ky, corresponding to a lower limit on the net aggradation rate of about 0.65 g/cm^2 ky. Given uncertainties in the measurements and with regard to the constancy of deposition with time, 0.50 g/cm^2 ky was used as the lower limit for the net aggradation rate. The grain-size distribution of the alluvial parent material is poorly sorted, making it difficult to quantify the amount of silt and carbonate accumulation within the profile, but it almost certainly is not more than an additional ~45 g/cm, yielding an upper limit to the estimated aggradation rate of 1.10 g/cm^2 ky.

A.3. Modeling of profile age and uncertainties

A primary purpose of the depth-profile approach is to constrain the inherited component of the cosmogenic nuclide inventory [29]. Inherited nuclides are those that were produced during erosion of the parent material and subsequent transport into the deposit sampled. The magnitude of the inherited component is determined by taking samples at depth, where cosmogenic production rates are negligible. This is the motivation for extending the sampling pits to ~3 m depth. In the case of Site 3, the smooth nature of the ^{36}Cl depth profile (Fig. 5B) rendered estimation of the inherited component relatively unambiguous. The best fit was for inheritance of 3.78×10^5 atoms ^{36}Cl/g. This inherited inventory was subtracted from all samples and was used uniformly in the fitting procedure. This inventory would be produced by exposure at the surface for 29 ka, at the elevation of the sample pit. This is the inherited inventory observed at the present time; the inventory at the time of deposition would have been about 21% greater due to radioactive decay of the ^{36}Cl in the intervening time (4.59×10^5 atoms ^{36}Cl/g, using the depositional age determined below).

The profile age and age uncertainty were calculated by means of χ^2 fitting [30] to modeled ^{36}Cl distribution with depth. The CHLOE program, employing the equations of [45], was the model and the free parameters were the profile age and the profile net erosion or aggradation rate. These two parameters were systematically varied in order to test the fit of the model to the data. Ages were allowed to range between 0 and whatever upper limit was necessary to exceed the χ^2 criteria, as described below. Erosion rate was varied between limits inferred from the particle-size analysis of the soils profile, as described above (e.g., net aggradation of 0.50 to 1.10 g/cm^2 ky for the profile at Silver

Canyon). The chi-squared function (χ^2) was calculated for each age-erosion pair as follows:

$$\chi^2 = \sum_{i=1}^{n} \frac{(O_i - M_i)^2}{S_i^2}$$

where O_i is the observed, normalized, ^{36}Cl concentration at each depth interval, i, and M_i is the modeled value at the same depth. The number of concentration measurements is n. S_i is the standard deviation associated with the ith data point.

$$S_i = S_{i,36} + S_{\text{inheritance}} + S_{\text{other}}$$

where $S_{i,36}$ is the standard deviation from the ^{36}Cl analytical measurement, $S_{\text{inheritance}}$ is the contribution to the standard deviation from variability in the inherited ^{36}Cl concentration, and S_{other} is the contribution from other sources of variability, principally analytical uncertainties in the chemical analyses, bulk densities, and other parameters, combined with uncertainties in the ^{36}Cl production parameters. $S_{i,36}$ was taken directly from the AMS analyses. $S_{\text{inheritance}}$ was estimated based on a depth-profile of ^{36}Cl concentration measured on a lacustrine beach deposit of known age (from radiocarbon chronology) formed by Lake Lahontan [42]. χ^2 fitting of the profile fitting yielded an age uncertainty that was 3% larger than theoretically calculated, assuming all other sources of variation were accounted for adequately. This enhancement of χ^2 can presumably be attributed to unaccounted-for variability of the inherited component. S_{other} was estimated based on an empirical comparison of ^{36}Cl ages with independently-constrained ages for 30 surficial rock samples [46] and was assigned a value of 7%.

The array of χ^2 values generated as described above was contoured. The best age estimate corresponds to the minimum value of χ^2. One-standard-deviation uncertainty bounds were estimated from the maximum and minimum age limits of the $\chi^2_{\text{min}} + \Delta\chi^2_{\text{v}}$ contour in the age-erosion parameter space. χ^2_{min} is the minimum value of the calculated χ^2 within the parameter space and $\Delta\chi^2_{\text{v}}$ is the critical value of the change in χ^2 for a specified level of confidence and number of fitted parameters (e.g., [54]) (Table 4). For our problem, the appropriate level of confidence is 68.3% (corresponding to one standard deviation and two fitted parameters, t and ε), giving a $\Delta\chi^2_{\text{v}}$ of 2.30.

The minimum in the χ^2 was found at 72 ka for an erosion rate of −0.7 g/cm^2 ky (i.e., an aggradation rate of 0.7 g/cm^2 ky) and an inheritance of 3.52×10^5 atoms ^{36}Cl/g (equivalent to 29 ky of exposure at the surface). At this combination of parameters, the χ^2 was 0.760 and the reduced χ^2 was 0.152. The variation in age necessary to raise the χ^2 to 3.01 (equal to $\chi^2_{\text{min}} + \Delta\chi^2_{\text{v}}$) was an approximately symmetrical 15 ky, with the upper critical point (88 ka) being at the lower aggradation limit (1.1 g/cm^2 ky) and the lower critical point (58 ka) being at the upper aggradation limit (0.5 g/cm^2 ky). Within any geologically-reasonable range of erosion or aggradation rates, the ages were relatively insensitive to the rates. Thus our best estimate of the age of the faulted alluvial fan surface at Silver Canyon is 72 ± 15 ka.

References

[1] S. Gupta, P.A. Cowie, N.H. Dawers, J.R. Underhill, A mechanism to explain rift-basin subsidence and stratigraphic patterns through fault-array evolution, Geology 26 (1998) 595–598.

[2] R.A. Bennett, A.M. Friedrich, K.P. Furlong, Codependent histories of the San Andreas and San Jacinto fault zones from inversion of fault displacement rates, Geology 32 (2004) 961–964.

[3] T.H. Dixon, E. Norabuena, L. Hotaling, Paleoseismology and global positioning system: earthquake-cycle effects and geodetic versus geologic fault slip rates in the Eastern California shear zone, Geology 31 (2003) 55–58.

[4] F. Pollitz, C. Wicks, W. Thatcher, Mantle flow beneath a continental strike-slip fault: postseismic deformation after the 1999 Hector mine earthquake, Science 293 (2001) 1814–1818.

[5] R.K. Dokka, C.J. Travis, Role of the Eastern California Shear Zone in accommodating Pacific–North America plate motion, Geophys. Res. Lett. 17 (1990) 1323–1326.

[6] M.C. Reheis, T.L. Sawyer, Late Cenozoic history and slip rates of the Fish Lake Valley, Emigrant Peak, and Deep Springs fault zone, Nevada and California, Geol. Soc. Amer. Bull. 109 (1997) 280–299.

[7] T.H. Dixon, M. Miller, F. Farina, H. Wang, D. Johnson, Present-day motion of the Sierra Nevada block and some tectonic implications for the Basin and Range province, North American Cordillera, Tectonics 19 (2000) 1–24.

[8] T.H. Dixon, S. Robaudo, J. Lee, M.C. Reheis, Constraints on present-day Basin and Range deformation from space geodesy, Tectonics 14 (1995) 755–772.

[9] M. Miller, D.J. Johnson, T.H. Dixon, R.K. Dokka, Refined kinematics of the Eastern California shear zone from GPS observations, 1993–1998, J. Geophys. Res. 106 (2001) 2245–2263.

[10] D.F. Stockli, T.A. Dumitru, M.O. McWilliams, K.A. Farley, Cenozoic tectonic evolution of the White Mountains, California and Nevada, Geol. Soc. Amer. Bull. 115 (2003) 788–816.

[11] M.C. Reheis, T.H. Dixon, Kinematics of the Eastern California shear zone: evidence for slip transfer from Owens and Saline Valley fault zones to Fish Lake Valley fault zone, Geology 24 (1996) 339–342.

[12] O. Bellier, M.L. Zoback, Recent state of stress change in the Walker Lane zone, western Basin and Range province, United States, Tectonics 14 (1995) 564–593.

[13] S.G. Wesnousky, C.H. Jones, Oblique slip, slip partitioning, spatial and temporal changes in the regional stress field, and the relative strength of active faults in the Basin and Range, western United States, Geology 22 (1994) 1031–1034.
[14] S.C. McClusky, S.C. Bjornstad, B.H. Hager, R.W. King, B.J. Meade, M.M. Miller, F.C. Monastero, B.J. Souter, Present day kinematics of the Eastern California Shear Zone from a geodetically constrained block model, Geophys. Res. Lett. 28 (2001) 3369–3372.
[15] S. Beanland, M.M. Clark, The Owens Valley fault zone, eastern California, and surface rupture associated with the 1872 earthquake, U.S. Geol. Surv. Bull. (1995) 29.
[16] J. Lee, J. Spencer, L. Owen, Holocene slip rates along the Owens Valley fault, California: implications for the recent evolution of the Eastern California Shear Zone, Geology 29 (2001) 819–822.
[17] S.N. Bacon, S.K. Pezzopane, R.M. Burke, Paleoseismology on the Owens Valley fault and latest quaternary stratigraphy in Owens Valley near Lone Pine, Eastern California, final technical report—National Earthquake Hazards Reduction Program (01-HQ-GR-0013 and 02-HQ-GR-0003), U.S. Geologic Survey, 2003, p. 42.
[18] C.M. DePolo, Seismotectonics of the White Mountains Fault System, East-central California and West-central Nevada, University of Nevada, 1989.
[19] A.M. Friedrich, B.P. Wernicke, N.A. Niemi, R.A. Bennett, J.L. Davis, Comparison of geodetic and geologic data from the Wasatch region, Utah, and implications for the spectral character of Earth deformation at periods of 10 to 10 million years, J. Geophys. Res. 108 (2003) 2199 (ETG 2197:2191-2123).
[20] S.B. Lueddecke, N. Pinter, P. Gans, Plio-Pleistocene ash falls, sedimentation, and range-front faulting along the White-Inyo Mountains front, California, J. Geol. 106 (1998) 511–522.
[21] P.C. Bateman, Geology and tungsten mineralization of the Bishop District California, U. S. Geol. Surv. Prof. Pap. 470 (1965) 208 (Washington, DC).
[22] A.M. Sarna-Wojcicki, M.S. Pringle, J. Wijbrans, New $^{40}Ar/^{39}Ar$ age of the Bishop Tuff from multiple sites and sediment rate calibration for the Matuyama-Brunhes boundary, J. Geophys. Res. 105 (2000) 21431–421443.
[23] K.J. Hollett, W.R. Danskin, W.F. McCaffrey, C.L. Walti, Geology and water resources of Owens Valley, California, U. S. Geol. Surv. Water-Supply Pap. (1991) 77 (Washington, DC).
[24] C.A. Nelson, C.A. Hall, W.G. Ernst, Geologic map of the central White-Inyo range, in: C.A. Hall (Ed.), Natural History of the White-Inyo Range, Eastern California, California Natural History guide, vol. 55, University of California Press, Berkeley, 1991.
[25] S.C. Thompson, R.J. Weldon, C.M. Rubin, K. Abdrakhmatov, P. Molnar, G.W. Berger, Late Quaternary slip rates across the central Tien Shan, Kyrgyzstan, central Asia, J. Geophys. Res. 107 (2002) 2203 (ETG 2207:2201-2232).
[26] J.W. Harden, E.M. Taylor, A quantitative comparison of soil development in four climatic regimes, Quat. Res. 20 (1983) 342–359.
[27] J.L. Slate, Quaternary stratigraphy, geomorphology, and geochronology of alluvial fans, Fish Lake Valley, Nevada-California, PhD, University of Colorado, 1992.
[28] P.H. Zehfuss, P.R. Bierman, A.R. Gillespie, R.M. Burke, M.W. Caffee, Slip rates on the Fish Springs Fault, Owens Valley, California, deduced from cosmogenic ^{10}Be and ^{26}Al and soil development on fan surfaces, Geol. Soc. Amer. Bull. 113 (2001) 241–255.
[29] R.S. Anderson, J.L. Repka, G.S. Dick, Explicit treatment of inheritance in dating depositional surfaces using in situ ^{10}Be and ^{26}Al, Geology 24 (1996) 47–51.
[30] P.R. Bevington, D.K. Robinson, Data Reduction and Error Analysis for the Physical Sciences, McGraw-Hill, New York, 1992, 328 pp.
[31] N.H. Dawers, M.H. Anders, Displacement–length scaling and fault linkage, J. Struct. Geol. 17 (1995) 607–614.
[32] T.W. Gardner, D.W. Jorgensen, C. Shuman, C.R. Lemieux, Geomorphic and tectonic process rates: effects of measured time interval, Geology 15 (1987) 259–261.
[33] J. Lee, C.M. Rubin, A. Calvert, Quaternary faulting history along the Deep Springs fault, California, Geol. Soc. Amer. Bull. 113 (2001) 855–869.
[34] T.K. Rockwell, S. Lindvall, M. Herzberg, D. Murbach, T. Dawson, G. Berger, Paleoseismology of the Johnson Valley, Kickapoo, and Homestead Valley faults: clustering of earthquakes in the Eastern California Shear Zone, Bull. Seismol. Soc. Am. 90 (2000) 1200–1236.
[35] A.R. Gillespie, Quaternary subsidence of Owens Valley, California, in: C.A. Hall (Ed.), Natural History of Eastern California and High-altitude Research 3, White Mountain Research Station Proceedings, Los Angeles, 1991, pp. 356–382.
[36] R. Hetzel, A. Hampel, Slip rate variations on normal faults during glacial–interglacial changes in surface loads, Nature 435 (2005) 81–84.
[37] C. Nostro, R.S. Stein, M. Cocco, M.E. Belardinelli, W. Marzochi, Two-way coupling between Vesuvius eruptions and southern Apennine earthquakes, Italy, by elastic stress transfer, J. Geophys. Res. 103 (1998) 24487–424504.
[38] W. Hildreth, G.A. Mahood, Ring-fracture eruption of the Bishop Tuff, Geol. Soc. Amer. Bull. 97 (1986) 396–403.
[39] G.R. Blake, Soil density, Amer. Soc. Agron., Monogr. Ser. 9 (1965) 374–390.
[40] D. Elmore, B.R. Fulton, M.R. Clover, J.R. Marsden, H.E. Gove, H. Naylor, K.H. Purser, L.R. Kilius, R.P. Beukens, A.E. Litherland, Analysis of ^{36}Cl in environmental water samples using an electrostatic accelerator, Nature 277 (1979) 22–25.
[41] P.F. Muzikar, D. Elmore, D.E. Granger, Accelerator mass spectrometry in geologic research, Geol. Soc. Amer. Bull. 115 (2003) 643–654.
[42] G. Kurth, Cosmogenic Nuclide Dating of Old, High Pluvial Shorelines in the Western Great Basin, M.S. New Mexico Institute of Mining & Technology, 2003.
[43] J.T. Fabryka-Martin, Production of radionuclides in the earth and their hydrogeologic significance, with emphasis on chlorine-36 and iodine-129, PhD, University of Arizona, 1988.
[44] F.M. Phillips, M. Zreda, M.R. Flinsch, D. Elmore, P. Sharma, A reevaluation of cosmogenic ^{36}Cl production rates in terrestrial rocks, Geophys. Res. Lett. 23 (1996) 949–952.
[45] J.C. Gosse, F.M. Phillips, Terrestrial in-situ cosmogenic nuclides: theory and application, Quat. Sci. Rev. 20 (2001) 1475–1560.
[46] F.M. Phillips, W.D. Stone, J.T. Fabryka-Martin, An improved approach to calculating low-energy cosmic-ray neutron fluxes near the land/atmosphere interface, Chem. Geol. 175 (2001) 689–701.
[47] J. Stone, J. Evans, K. Fifield, R. Cresswell, G. Allan, Cosmogenic chlorine-36 production rates from calcium and potassium, Radiocarbon 38 (1996) 170–171.

[48] J.O. Stone, G.L. Allan, L. Fifield, K., R.G. Cresswell, Cosmogenic chlorine-36 from calcium spallation, Geochim. Cosmochim. Acta 60 (1996) 679–692.
[49] W.B. Bull, Geomorphic Response to Climate Change, Oxford Press, New York, 1991, 326 pp.
[50] P.W. Birkeland, Soils and Geomorphology, Oxford University Press, Oxford, 1999, 430 pp.
[51] C.A. Stiles, C.I. Mora, S.G. Driese, A.C. Robinson, Distinguishing climate and time in the soil record: mass-balance trends in Vertisols from the Texas coastal prairie, Geology 31 (2003) 331–334.
[52] L.D. McFadden, E.V. McDonald, S.G. Wells, K. Anderson, J. Quade, S.L. Forman, The vesicular layer and carbonate collars of desert soils and pavements: formation, age, and relation to climate change, Geomorphology 24 (1998) 101–145.
[53] J.C. Dohrenwend, S.G. Wells, B.D. Turrin, Degradation of Quaternary cinder cones in the Cima volcanic field, Mojave Desert, California, Geol. Soc. Amer. Bull. 97 (1986) 421–427.
[54] J.C. Davis, Statistics and Data Analysis in Geology, John Wiley & Sons, New York, 2002, 638 pp.